ELSEVIER

Contents lists available at ScienceDirect

Materials & Design

journal homepage: www.elsevier.com/locate/matdes



Elastic behavior of binary and ternary refractory multi-principal-element alloys



Rui Feng ^a, George Kim ^b, Dunji Yu ^a, Yan Chen ^a, Wei Chen ^b, Peter K. Liaw ^c, Ke An ^{a,*}

- ^a Neutron Scattering Division, Oak Ridge National Laboratory, Oak Ridge, TN 37831, United States
- ^b Department of Mechanical, Materials, and Aerospace Engineering, Illinois Institute of Technology, Chicago, IL 60616, United States
- ^c Department of Materials Science and Engineering, The University of Tennessee, Knoxville, TN 37996, United States

HIGHLIGHTS

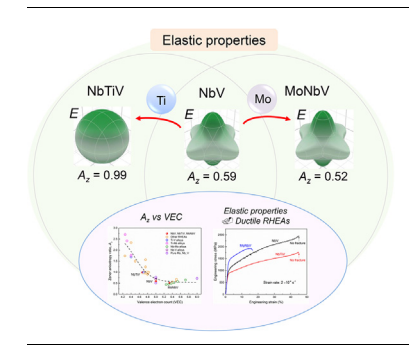
- In-situ neutron diffraction measured the elastic properties of NbV, NbTiV, and MoNbV alloys, which are consistent with first-principles calculations.
- Adding Ti elements into the NbV alloy results in the formation of the elastically isotropic NbTiV alloy.
- This work provides valuable insights into the design of ductile and strong refractory high-entropy alloys by tuning the elastic properties.

ARTICLE INFO

Article history: Received 30 March 2022 Revised 17 May 2022 Accepted 2 June 2022 Available online 6 June 2022

Keywords:
Multi-principal-element alloys
Elastic properties
Neutron diffraction
First-principles calculations
Mechanical behavior

G R A P H I C A L A B S T R A C T



ABSTRACT

Elastic properties are essential to the mechanical performance of materials, and therefore, can be tuned to design high-performance materials. In this study, the elastic constants of the equiatomic ternary refractory multi-principal-element alloys, NbTiV, and MoNbV, were investigated, using *in-situ* neutron diffraction and first-principles calculations. The experimentally measured and theoretically predicted elastic constants show a good agreement. The alloying effect of adding Ti and Mo into NbV base alloy on the elastic constants is studied. Particularly, adding Ti elements into the NbV alloy results in the increase of the Zener anisotropy ratio from 0.59 to 0.99, leading to the formation of the elastically isotropic NbTiV alloy, while the addition of Mo decreases the anisotropy ratio to 0.52. Pugh's ratio (B/G), Cauchy pressure (C_{12} - C_{44}), and Poisson's ratio (V) are used to predict the brittle/ductile nature of the studied alloys, which is consistent with the mechanical results. The present work provides valuable insights into the design of ductile and strong refractory high-entropy alloys by tuning the elastic properties.

© 2022 The Authors. Published by Elsevier Ltd. This is an open access article under the CC BY license (http://creativecommons.org/licenses/by/4.0/).

1. Introduction

High-entropy alloys (HEAs) or multi-principal-element alloys (MPEAs) are a class of alloys that are chemically concentrated and focus on the less explored central regions of multi-element phase diagrams [1–5]. Due to the absence of an obvious base

* Corresponding author. E-mail address: kean@ornl.gov (K. An). element, HEAs have a near-infinite compositional space in which to discover high-performance materials. Many unique and promising properties have been found in HEAs, such as their high strength and good ductility [6–11], great fatigue/fracture resistance [12,13], outstanding corrosion resistance [14,15], attractive magnetic properties [16–18], etc. Among several classes of HEAs, refractory HEAs (RHEAs) have attracted tremendous interest because of their outstanding high-temperature strength, providing potential for greatly enhanced performance

of high-temperature structural materials in the aerospace industries [3.19].

Elastic behavior is one of the intrinsic properties of materials. As a measure of resistance to separation or shear of adjacent atoms, elastic properties are directly related to the mechanical performance of alloys and are important parameters to understand their strengthening and ductility behavior [19,20]. Thus, the elastic constants, e.g., Young's modulus (E), shear modulus (G), bulk modulus (B), and Poisson's ratio (v), can be used as input data in a variety of theoretical models to discuss and predict the mechanical performance of materials. For example, elastic information of Pugh's ratio (B/G), Cauchy pressure, and Poisson's ratio can be used to predict the brittle-ductile characteristic of materials [21,22]. temperature-dependent elastic moduli of materials are of significance for understanding their temperature-dependent strength. which can be served as a critical criterion when designing highperformance structural materials resistant to high temperatures, such as RHEAs. Several single body-centered cubic (BCC) RHEA systems with attractive high-temperature strength have been reported in previous works [6,23,24]. For example, MoNbTaVW, NbTaTiV, and CrMoNbV RHEAs are good model alloys showing the efficacy of selecting refractory elements with the weak temperature dependence of elastic constants, such as Nb and V, to achieve high strengths at elevated temperatures [6,23,24]. Therefore, studying the elastic properties of these model alloys including their subsystems can provide useful guidelines for the design of high-performance RHEAs that are based on them. While most of the reported works are for quaternary and quinary equiatomic systems, to our knowledge, the elastic properties of the ternary equiatomic alloys were rarely reported on. In particular, the ternary NbTiV and MoNbV alloys are the critical subsystems of those model RHEAs with outstanding properties [6,23,24]. Thus, in this study, we fabricated and investigated the elastic properties of the equiatomic NbTiV, and MoNbV MPEAs from the NbV base alloy. Their elastic properties including NbV were investigated by the state-of-the-art in-situ neutron diffraction and predicted by first-principles calculations. Particularly, it is found that the NbTiV alloy shows elastically isotropic characteristics, with a Zener anisotropy ratio of 0.99. The present work could offer guidance to design ductile and strong RHEAs.

2. Materials and Methods

2.1. Sample preparation, characterization, and mechanical tests

The NbV, NbTiV, and MoNbV MPEAs with equiatomic ratios were fabricated by arc-melting pure raw elements with purity > 99.9% weight percent (wt.%), and then drop casting into a water-cooled copper hearth. To ensure a homogenous chemical distribution, the melting and solidification processes were repeated at least eight times. The NbV and NbTiV samples were further homogenized at 1200 °C for 3 days and 1 day, respectively, which were encapsulated in a quartz tube with a vacuum of $\sim 2\times 10^{-2}$ mbar. The MoNbV sample was annealed at 1400 °C for 3 h under a vacuum of $\sim 10^{-6}$ mbar using a vacuum furnace, where a heating rate of 25 °C/min and a furnace cooling with an initial cooling rate of 80 °C/min were employed.

The microstructures of the three alloys were characterized by scanning-electron microscopy (SEM), using a TESCAN MIRA3 FEG-SEM coupled with back-scattering electron (BES) and energy-dispersive spectroscopy (EDS) detectors. The specimens for SEM characterization were initially polished to a mirror finish

employing the 1200-grit SiC paper, followed by a vibratory polishing, using the 0.05 mm SiC suspension.

The compression tests were conducted on the cylindrical specimens of the studied alloys (3 mm in diameter and 6 mm in length) at room temperature (RT) with a strain rate of 2 \times 10 $^{-4}$ s $^{-1}$, using an MTS Model 810 servo-hydraulic machine.

2.2. In-situ neutron diffraction and the determination of elastic constants

In-situ neutron diffraction experiments subjected to compression were performed at RT, using an MTS load frame on the VUL-CAN Engineering Materials Diffractometer at the Spallation Neutron Source (SNS), Oak Ridge National Laboratory (ORNL) [25,26]. The cylindrical specimens with a diameter of 5 mm and a length of 10 mm were used. A continuous displacement control model was employed during the in-situ neutron measurements. The neutron-diffraction spectra were collected simultaneously by two detector banks in VULCAN, which are from grains whose lattice planes (hkl) were along and perpendicular to the loading axis. The collected data were reduced and analyzed, employing the VUL-CAN Data Reduction and Interactive Visualization softwarE (VDRIVE) [27]. The hkl plane-specific lattice strain of each respective phase is determined by $arepsilon_{hkl} = \left(d_{hkl} - d_{hkl}^0\right)/d_{hkl}^0$, where d_{hkl}^0 and d_{hkl} are the reference lattice d-spacing in the stress-free state and the lattice *d*-spacing during loading, respectively.

Single-crystal elastic constants can be determined by *in-situ* neutron diffraction results during mechanical loading of polycrystalline materials, using theoretical models, such as Kroner model [28]. When the specimen is loaded uniaxially in the elastic regime, each hkl-specific lattice strain as a function of the applied stress in the longitudinal and transverse directions can be measured, respectively. Consequently, the hkl-specific reciprocal diffraction elastic constants, $1/E_{hkl}$ and v/E_{hkl} , can be experimentally obtained. Using Kroner model [28,29], $1/E_{hkl}$ and v/E_{hkl} , can be calculated by setting single-crystal elastic constants, C_{ij} , as free parameters from the following Eqs. (1) and (2). Eventually, the single-crystal elastic constants, C_{ij} , are determined by the least-squares fittiWhen the specimen is loaded uniaxially in the elastic regimeng by Eq. (3).

$$\frac{1}{9B} - \frac{1}{6G_{hkl}} = -\frac{\nu_{hkl}}{E_{hkl}}$$

$$\frac{1}{G_{hkl}} = 2\left(\frac{1}{E_{hkl}} + \frac{v_{hkl}}{E_{hkl}}\right)$$

$$\begin{split} \chi^2 &= \sum_{i=1}^{n} \left((1/E_{hkl})_{\text{exp},i} - (1/E_{hkl})_{\text{mod el},i} \right)^2 / e_{1,i}^2 \\ &+ \left((\nu_{hkl}/E_{hkl})_{\text{exp},i} - (\nu_{hkl}/E_{hkl})_{\text{mod el},i} \right)^2 / e_{2,i}^2 \end{split}$$

where B is the bulk modulus, which is equal to $(C_{11} + 2C_{12})/3$; E_{hkl} , v_{hkl} , and G_{hkl} are hkl specific Young's moduli, Poisson's ratios, and shear moduli, respectively; n is the number of (hkl) diffraction planes used to fit Kroner model; $(1/E_{hkl})_{\rm exp}$ and $(v_{hkl}/E_{hkl})_{\rm exp}$ are determined from the in-situ neutron-diffraction results; e_1 and e_2 are the corresponding experimental errors; and $(1/E_{hkl})_{\rm model}$ and $(v_{hkl}/E_{hkl})_{\rm model}$ are calculated, using the model.

2.3. First-principles calculations

First-principles calculations were performed with the Vienna Ab-initio Simulation Package (VASP) to calculate the single-crystal elastic constants [30,31], using the projector augmented wave (PAW) method [32]. The exchange-correlation energy was

described with the generalized gradient approximation (GGA) in the Perdew-Becke-Ernzehof (PBE) parameterization [33]. A plane-wave cutoff of 520 eV, and Monkhorst-Pack k-point meshes with a density of 5000 k-points per reciprocal atom were used for all calculations. All structures were optimized until the energy was converged within 10^{-5} eV per supercell. The chemical disorder was modeled with special quasi-random structures (SQS) [34]. The SQS were generated using the mcsqs code from the Alloy Theoretic Automated Toolkit (ATAT) which uses a Monte Carlo algorithm with an objective function to find the closest match of correlation functions of a disordered state [35]. The convergence of elastic constants was tested with a series of SQS with different sizes. Multiple supercells (36-atom and 54-atom SQS structures for NbTiV and MoNbV alloys, and 48-atom and 54 atom SQS structures for NbV alloy) for each composition are generated.

The elastic tensor was calculated, using a computational workflow based on the stress–strain method described in Ref. [36]. Starting with a relaxed SQS of the HEA, a set of distorted structures were generated, employing 3×3 Green-Lagrange strain tensors of varying magnitudes at \pm 0.5% and \pm 1%. For each distorted structure, the 3×3 stress tensor is computed by DFT. The elastic tensor of the SQS is calculated from the relationship between the stress and strain tensors. More details can be found in Ref. [37].

3. Results and discussion

The phase structures and the microstructures of NbV, NbTiV, and MoNbV alloys were characterized by neutron diffraction and SEM, respectively. As shown in Fig. 1a, all three alloys exhibit a single BCC structure. From the calculated lattice parameters (NbV: a = 3.1788 Å; NbTiV: a = 3.2056 Å; MoNbV: a = 3.1612 Å) by Rietveld refinements, one can notice that the addition of Ti into the binary NbV alloy results in an increase in the lattice parameter, while the

addition of Mo leads to a slight decrease in the lattice parameter. This trend is due to the relatively large atomic radius of Ti (r = 1. 46 Å) and the small atomic radius of Mo (r = 1.4 Å), respectively, compared to that of the base NbV (Nb, r = 1.47 Å; V, r = 1.35 Å; average, r = 1.41 Å). One can also notice the different intensity scales of the hkl indexes among the three alloys, which is due to their different coherent neutron scattering sections. The SEM BSE images (Fig. 1b-c) display that the equiaxed BCC grains are present in NbV and NbTiV alloys after annealing at 1200 °C, revealing that recrystallization occurred in both alloys. However, after annealing at 1400 °C for 3 h, MoNbV alloy still presents a typical dendritic microstructure (Fig. 1d), where the dendritic region is enriched with Mo, while the interdendritic region is segregated with V, and Nb is relatively uniform in both regions (Fig. 1e). This result suggests that Mo with high-melting points solidifies first, while V with low-melting points crystalizes later during the solidification. The inhomogeneous chemical distribution also suggests that either the homogenization temperature needs to be higher or the annealing time needs to be longer for achieving a chemical homogeneous distribution for MoNbV.

Fig. 2a-c present the relationships of the applied stress as a function of the lattice strain of the three alloys along the loading and transverse directions (LD and TD). Within the elastic regime, a linear response of the lattice strain to the applied stress is found in the three alloys. For the linear relationship, different slopes among the various (hkl) grain families indicate elastic anisotropy. In NbV and MoNbV, the curves of the (200) and (211) lattice grains exhibit the highest and lowest slopes with a clear split, i.e., the highest and lowest directional strength-to-stiffness ratios, respectively. This trend indicates that an obvious elastically anisotropic characteristic exists in NbV and MoNbV. Interestingly, in NbTiV, the slopes of different grain families are almost the same in the linear-elastic region, suggesting elastic isotropy. From the

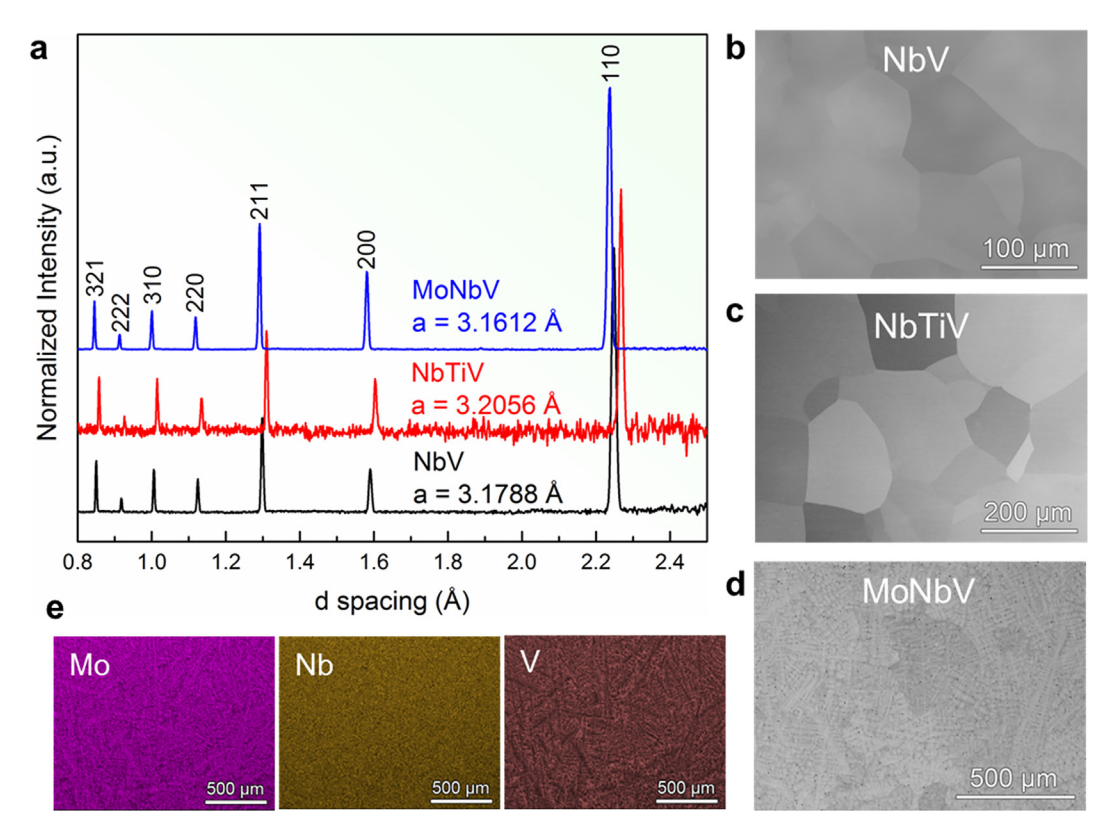


Fig. 1. Phases and microstructures of NbV, NbTiV, and MoNbV. (a) Neutron-diffraction patterns of the studied alloys at RT. (b-d) BSE SEM images of NbV, NbTiV, and MoNbV, respectively. (e) EDS elemental maps of MoNbV.

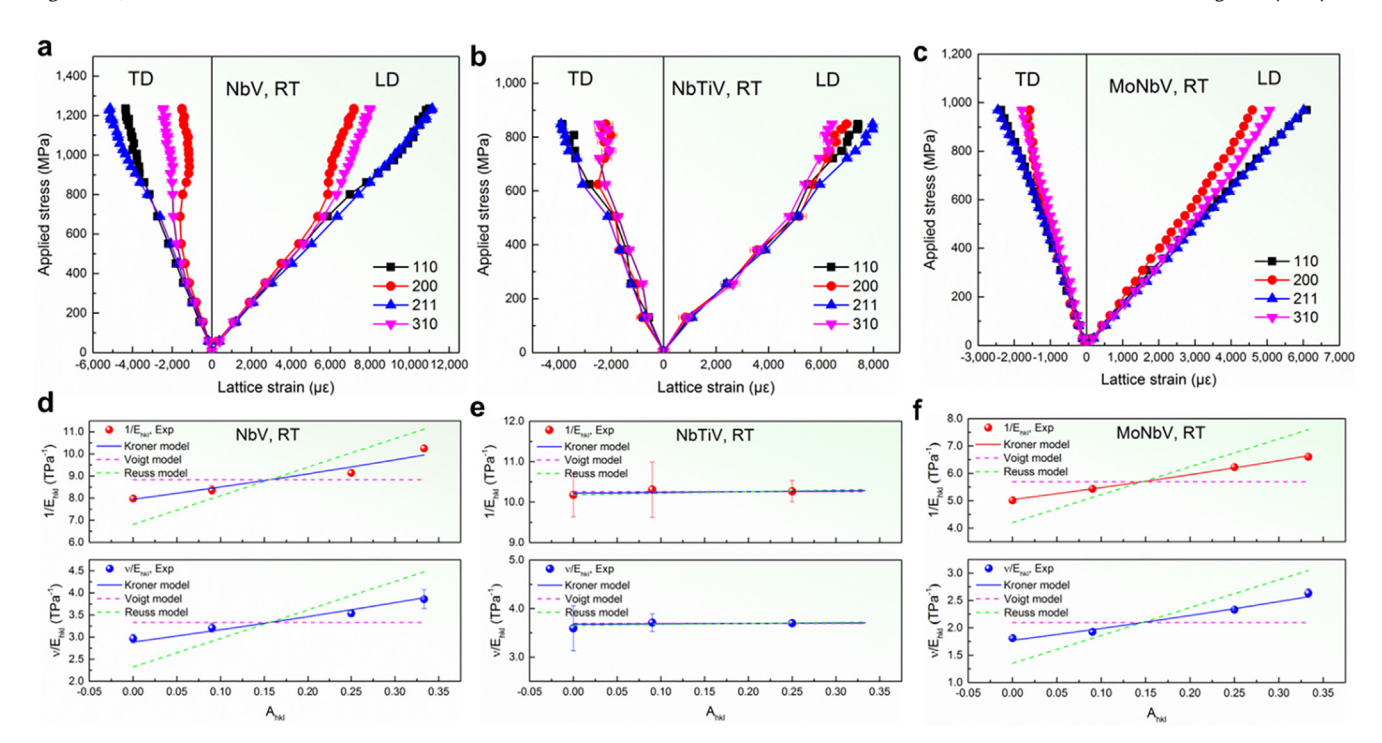


Fig. 2. Relationship of lattice strains vs. applied stress and reciprocal diffraction elastic constants, v_{hkl}/E_{hkl} and $1/E_{hkl}$, as a function of the elastic anisotropy factor, A_{hkl} , for NbV, NbTiV, and MoNbV alloys at RT. (**a-c**) Lattice-strain responses of {110}, {200}, {211}, and {310} crystallographic orientations with respect to the applied compressive stress along the loading and transverse directions of the studied alloys during the elastic deformation. (**d-f**) The reciprocal diffraction elastic constants, v_{hkl}/E_{hkl} and $1/E_{hkl}$, (symbols) as a function of the elastic anisotropy factor, A_{hkl} , for NbV, NbTiV, and MoNbV alloys, respectively, which are fitted by Kroner model (solid lines) and by Reuss and Voigt models (dash lines).

linear relationship in the elastic regime, the diffraction elastic constants, E_{hkl} and v_{hkl} , were determined, which were used to calculate the single-crystal elastic constants, Cij, using Kroner model. Note that the observed inhomogeneous chemical distribution in MoNbV alloy has a negligible influence on the elastic results because of the coherent interfacial relationship between the dendritic and interdendritic regions during elastic loading (see Supplementary Fig. S1). Fig. 2d-f plot the reciprocal diffraction elastic constants, $1/E_{hkl}$ and v_{hkl}/E_{hkl} , as a function of the elastic anisotropy factor, $A_{hkl}=\left(\frac{h^2k^2+k^2l^2+l^2h^2}{(h^2+k^2+l^2)^2}\right)$ as well as the ones fitted by Kroner, Voigt, and Reuss models for the studied alloys [38]. Kroner model fits the experimental data better, compared to Voigt and Reuss models. The elastic constants of C_{11} , C_{12} , and C_{44} that are determined by Kroner model are listed in Table 1. The single-crystal elastic constants predicted by the first-principles calculations are also given in Table 1.

Using the calculated single-crystal elastic constants, the polycrystalline elastic constants, e.g., Young's modulus (E), shear modulus (G), bulk modulus (B), and Poisson's ratio (v), can be estimated according to the Voigt-Reuss-Hill (VRH) averaging approximation [39]. The polycrystalline shear modulus (G) is defined as.

$$G = \frac{(G_V + G_R)}{2}$$

where G_V and G_R are Voigt and Reuss shear moduli, respectively, standing for the upper and lower limits of shear moduli, which are given by $G_V = \frac{(C_{11} - C_{12}) + 3C_{44}}{S}$ and $G_R = \frac{5(C_{11} - C_{12}) C_{44}}{3(C_{11} - C_{12}) + 4C_{44}}$, respectively. Therefore, B, E, and V can be calculated from the following equations.

$$B = \frac{C_{11} + 2C_{12}}{3}$$

$$E = \frac{9BG}{3B + G}$$

$$v = \frac{3B - 2G}{6B + 2G}$$

Based on the above equations, the experimentally-measured and DFT-predicted polycrystalline moduli (E, G, B, and v) of NbV, NbTiV, and MoNbV are obtained and listed in Table 1. Among the three alloys, MoNbV has the largest E, G, and B values, and NbTiV has the smallest E, G, and B values. This trend is due to the additions of Mo and Ti into NbV, which make the alloys tend to behave

Table 1Neutron-diffraction measured and first-principles calculation predicted single-crystal constants (C_{11} , C_{12} , and C_{44}), Zener anisotropy ratio (A_Z), macroscopic elastic moduli [Young's modulus (E/GPa), shear modulus (E/GPa), bulk modulus (E/GPa)], and Poisson's ratio (v) of the studied NbV, NbTiV, and MoNbV alloys.

Methods	Alloys	C ₁₁ (GPa)	C ₁₂ (GPa)	C ₄₄ (GPa)	C_{12} - C_{44}	A_z	E (GPa)	G (GPa)	B (GPa)	ν	B/G
In-situ neutron	NbV	226.7	117.4	32.0	85.4	0.59	109.7	39.7	153.8	0.381	3.87
diffraction	NbTiV	164.4	92.1	35.6	56.5	0.99	97.4	35.8	116.2	0.360	3.25
	MoNbV	342.3	162.2	47.0	115.2	0.52	167.9	61.1	223.1	0.375	3.65
DFT	NbV	220.3 ± 9.3	150.7 ± 6.8	35.6 ± 4.0	115.1 ± 7.9	1.07 ± 0.28	98.3 ± 6.0	35.0 ± 2.3	173.9 ± 3.0	0.406 ± 0.006	4.99 ± 0.35
	NbTiV	184.3 ± 8.3	126.1 ± 4.2	29.9 ± 2.8	96.2 ± 5.0	1.05 ± 0.15	82.8 ± 9.9	29.5 ± 3.8	145.5 ± 0.8	0.405 ± 0.011	4.99 ± 0.64
	MoNbV	292.6 ± 4.0	154.1 ± 8.8	56.7 ± 7.0	97.4 ± 11.2	0.83 ± 0.18	166.7 ± 6.9	61.2 ± 2.7	200.3 ± 4.9	0.361 ± 0.005	3.28 ± 0.13

more like pure Mo and Ti that have the largest and smallest E, G, and B values, respectively, among the pure Mo, Nb, Ti, and V elements. In contrast, the additions of Mo and Ti into NbV do not result in a clear change in Poisson's ratio (v). Fig. 3 plots a direct comparison of the elastic constants between the experimental and the predicted results of the studied alloys. It can be seen that a good agreement is obtained from the experimental and calculated results. The small difference between them can be ascribed to the different conditions under which these results are obtained. In the DFT calculations, an ideal BCC solid-solution phase at 0 K is modeled. However, in the experimental samples, there is a finite temperature effect, and some degree of short-range ordering (SRO) could exist, resulting in a deviation from such an ideal solid-solution condition in the modeling.

Three-dimensional (3D) surfaces of the crystallographic-orienta tion-dependent Young's and shear moduli, and Poisson's ratios are plotted to show the extents of the elastic anisotropy in the studied alloys (Fig. 4) [40]. The 3D surfaces of NbV and MoNbV have similar shapes. From the E_{hkl} plots of NbV and MoNbV (Fig. 4a and 4 g), it can be observed that $\langle 100 \rangle$ is the stiffest orientation, and the $\langle 111 \rangle$ is the most compliant direction, analogous to the elastic properties of pure elements of Nb and Mo. In NbTiV, the 3D contour plots of the Young's and shear moduli, and Poisson's ratios exhibit a nearly perfect spherical shape, indicating that NbTiV is elastically isotropic. Typically, elastic anisotropy is expressed by the Zener anisotropy ratio, $A_z = 2C_{44}/(C_{11}-C_{12})$, where $A_z = 1$ means elastic isotropy and any departure from unity indicates the degree of elastic anisotropy [41]. Based on the determined C_{11} , C_{12} , and C_{44} from neutron diffraction results (Table 1), the Zenner anisotropy ratio, A_z , of NbTiV is calculated as 0.99, which agrees well with the DFT-predicted one with the smallest standard deviation (1.05 ± 0.15). In contrast, NbV and MoNbV show strong elastic anisotropy, as evidenced by their anisotropy ratios of 0.59 and 0.52, respectively. From Table 1, it is worth noting that the DFTpredicted anisotropy ratios of NbV and MoNbV are different from those determined by neutron diffraction. This is because that A_{z} is highly sensitive to both C_{11} - C_{12} , and C_{44} . Even small variances in predicted elastic constants (less than 10 GPa) can lead to large changes in A_7 . Fig. 5 plots the relationship between the Zener anisotropy ratio, A_z , and valence electron concentration (VEC) of the studied alloys, in which values for pure Mo, Nb, V [42,43], other RHEAs [6,44-50], and some related BCC transition metal alloys [42,51–56] are also included for the comparison. It can be seen

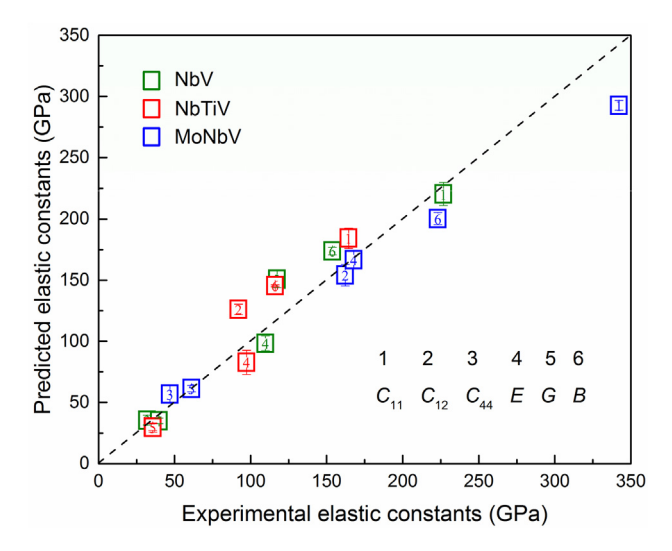


Fig. 3. Comparison of experimental and predicted elastic constants of the studied NbV, NbTiV, and MoNbV alloys.

that, in general, the Zener anisotropy ratio decreases with the increase of the VEC value. It should be emphasized that several elastically isotropic HEAs, including the studied NbTiV alloy, are found with a VEC value of about 4.7 (highlighted by the orange background), which is consistent with previous reports [48,57,58]. It is good to clarify that the trend of elastically isotropic materials with VEC \sim 4.7 is just an observed correlation rather than an explained causation [59]. The VEC value is related to the suitable number of valence electrons in the outmost shell of the alloys, which may weaken the directional bond strength and lead to isotropically elastic behavior. However, this trend could still provide useful guidance to design elastically isotropic HEAs via rationally adjusting chemical compositions for achieving a VEC \sim 4.7, particularly, by mixing copper-like transition metals $(A_z > 1)$, e.g., Al, Ta, Ti, and Zr, and niobium-like transition metals (A_7 less than 1), e.g., Cr. Mo. Nb. and V.

Another facet to consider is the comparison of lattice distortion between NbTiV and MoNbV alloys which arise from the atomic size mismatches of the constituent elements. Fig. 6a-c show the spread of 1st nearest neighbor (NN) distances of different pairs of atomic species for NbV, NbTiV, and MoNbV alloys respectively. The large spread range of the atomic pair distribution, i.e., the range of box and whisker plots in Fig. 6, can be a metric for a severe local lattice distortion. The atomic pairs containing Mo (Mo-Mo, Mo-Nb, Mo-V) tend to have smaller 1st NN bond lengths compared to the atomic pairs containing Ti (Ti-Ti, Ti-Nb, Ti-V). Considering the BCC structures of Ti and Mo, DFT calculated 1st NN distances of Ti and Mo are 2.816 and 2.743 Å respectively. These values are actually in good agreement with the median and mean 1st NN distances of Ti-Ti, and Mo-Mo pairs in Fig. 6b and 6c. It also seems that the range of 1st NN distances is larger with the addition of Ti to the Nb-V binary system compared to the addition of Mo, resulting in a slightly larger amount of lattice distortion in NbTiV. However, the correlation between increased lattice distortion and isotropy in NbTiV may be coincidental, as this investigation by Yen et al. [60] in lattice distortion and elastic anisotropy suggests that lattice distortion only has a minor effect on elastic anisotropy and that lattice distortion tends to increase elastic anisotropy, rather than decrease it. The connection between lattice distortion and elastic isotropy is a relationship that could be a new factor to elucidate for HEA design, but it still needs future research to understand.

The brittle-ductile characteristic of a material can be predicted, using criteria such as Pugh's ratio (B/G), Cauchy pressure (C_{12} - C_{44}), and Poisson's ratio (v) [21,22,61–63]. Bulk modulus (B) describes the response to the hydrostatic pressure, reflecting the bonding strength between atoms and the resistance to cleavage. A large B can minimize the volume expansion, thus resist the void formation and result in large plastic deformation. The shear modulus, G, reflects the resistance against the dislocation movement. A small *G* results in an easy dislocation slip, leading to a large plastic strain. According to Pugh's criterion, when B/G > 1.75, the alloy usually shows ductility [21], and the larger the B/G is, the better the ductility is. Otherwise, it intends to be brittle. As reflected in Eq. 7, the Poisson's ratio, v, is linked with B/G, with $\frac{B}{G} = \frac{2(1+v)}{3(1-2v)}$. Therefore, it is readily seen that a high B/G value corresponds to a high Poisson's ratio, resulting in a critical value of 0.26 of the Poisson's ratio for the brittle-to-ductile transition. According to the data listed in Table 1, the experimental and predicted *B*/*G* values of NbV, NbTiV, and MoNbV are larger than the critical value of B/G = 1.75, and the values of the Poisson's ratio is > 0.26, indicating the ductile nature of the studied alloys. Moreover, Cauchy pressure, $(C_{12}$ - $C_{44})$, that reflects the character of atomic bonding is often used to evaluate ductility. A negative Cauchy pressure means a covalent bond accompanied by brittle behavior, while a positive Cauchy pressure corresponds to a metallic bond with ductile behavior. The positive

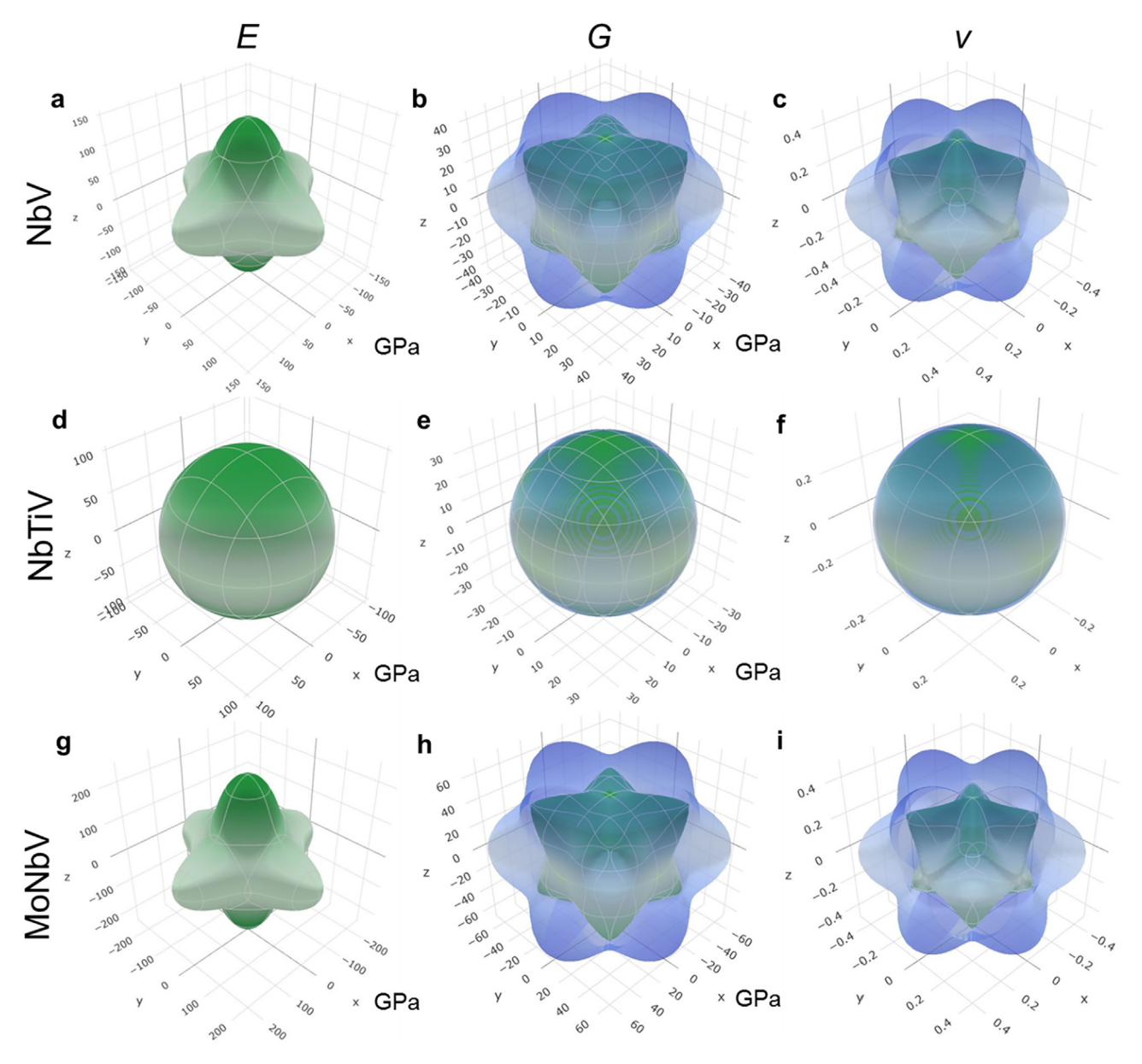


Fig. 4. Spatial dependence of Young's and shear moduli and Poisson's ratio of NbV, NbTiV, and MoNbV at RT. (a-c) 3D visualization of Young's moduli, shear moduli, and Poisson's ratio of NbV, respectively. (d-f) 3D visualization of Young's moduli, shear moduli, and Poisson's ratio of NbTiV, respectively. (g-i) 3D visualization of Young's moduli, shear moduli, and Poisson's ratios of the MoNbV alloy, respectively. The X, Y, Z axes correspond to the three orthogonal axes, [100], [010], and [001] directions, respectively. The transparent blue outer surfaces and the solid green inner surfaces in the figures represent the positive maximum and minimum values of shear moduli and Poisson's ratios, respectively. (For interpretation of the references to colour in this figure legend, the reader is referred to the web version of this article.)

Cauchy pressure indicates that the metallic bonds are in the studied alloys, suggesting the ductile nature. The predicted ductile nature of the three alloys agrees well with the compressive strains of NbV (> 50%), NbTiV (> 50%), and MoNbV (\sim 15%) in Fig. 7.

Alloying effects on the evolution of elastic constants can be understood from the present work, which could offer valuable insights into the design of novel HEAs by alloying elements. When going from binary NbV to ternary NbTiV and MoNbV, we can see the effect of alloying Ti and Mo on the elastic constants. Table 2 summarizes the changes in the elastic constants measured by neutron diffraction for NbTiV and MoNbV, relative to NbV. The addition of Ti into NbV causes a decrease in C_{11} and C_{12} , but C_{44} has a slight increase. For alloying with Mo, C_{11} , C_{12} , and C_{44} are all strongly enhanced, particularly, a 115.6 GPa increase in C_{11} . The effect of alloying Ti and Mo into NbV on the changes of elastic constants can be understood from the individual elastic constants of

Ti, Mo, and NbV. Table 3 summarizes the elastic properties of the pure constituent elements, and other related RHEAs that are based on the studied binary and ternary alloys [6,43-50,64,65]. As shown in Table 3, Ti has lower C_{11} and C_{12} values, but higher C_{44} values than those of NbV. However, the values of C_{11} , C_{12} , and C_{44} in pure Mo are all much higher than those of NbV. Particularly, the C_{11} is about 243 GPa higher than that of NbV. Therefore, the alloying effect by Ti and Mo on the elastic constants can be understood by comparing the elastic constants of pure Ti and Mo to those of the NbV host. In addition to the effect on elastic constants, the alloying effect on the B/G ratio and Poisson's ratio are also evaluated. The differences in *B/G* ratio and Poisson's ratio of NbV, NbTiV, and MoNbV determined from the neutron-diffraction results are small, but a clear decrease of both the B/G ratio and Poisson's ratio from the DFT-predicted data occur in MoNbV (Table 1), suggesting that reduced ductility could occur in MoNbV. Observing their

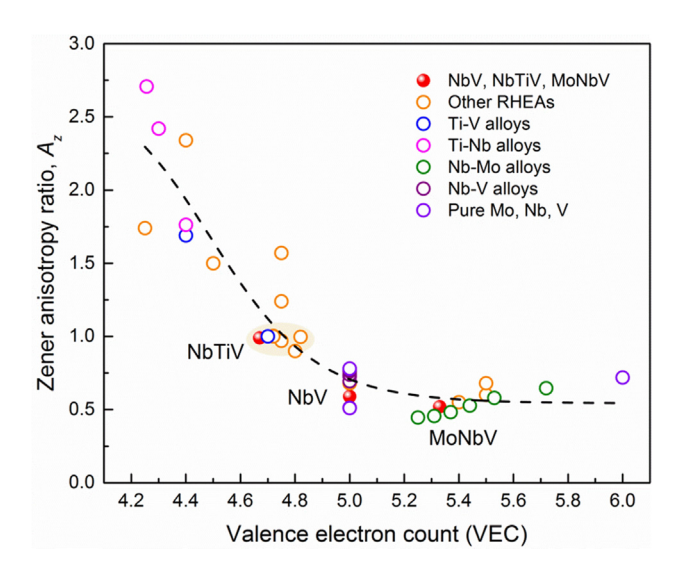


Fig. 5. Zener anisotropy ratio, A_2 , as a function of valence electron count (VEC) for the studied NbV, NbTiV, and MoNbV alloys, and other reported RHEAs [6,44–50], Ti-V alloys [51,52], Ti-Nb alloys [53–55], Nb-Mo alloys [42], Nb-V alloys [56], and pure Mo, Nb, and V [42,43].

compressive stress–strain curves (Fig. 7), we can notice that NbV and NbTiV have large compressive strains (> 50%) with yield strengths of 910 MPa and 809 MPa, respectively, while MoNbV has a decreased compressive strain of \sim 15% with a greatly enhanced yield strength of 1260 MPa. The tendency toward increased strength and brittleness in MoNbV can be attributed to the relatively brittle nature of Mo (B/G = 2.19, Table 3), and the

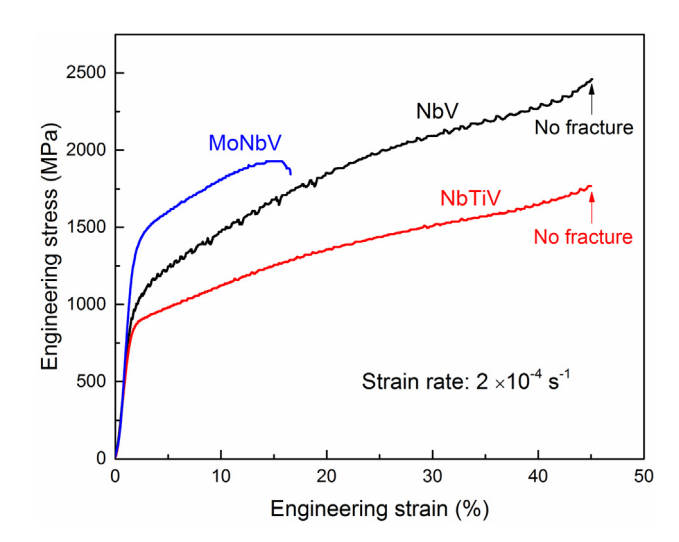


Fig. 7. Compressive engineering stress-strain curves of the studied NbV, NbTiV, and MoNbV alloys at RT.

small atomic radius (r = 1.4 Å) and shear modulus (20 GPa) of Mo, resulting in large atomic-size and modulus mismatches [6].

Furthermore, from ternary to quaternary alloys, the effect of alloying elements on the elastic and mechanical properties can be explained, based on the present work and the data collected from the literature. In Table 3, when going from ternary NbTiV and MoNbV to the quaternary NbTiVZr, MoNbTiV, and AlMoNbV, CrMoNbV, respectively, the values of the *B*/*G* ratio decrease, indicating that adding Zr and Mo to NbTiV, and Al and Cr to MoNbV

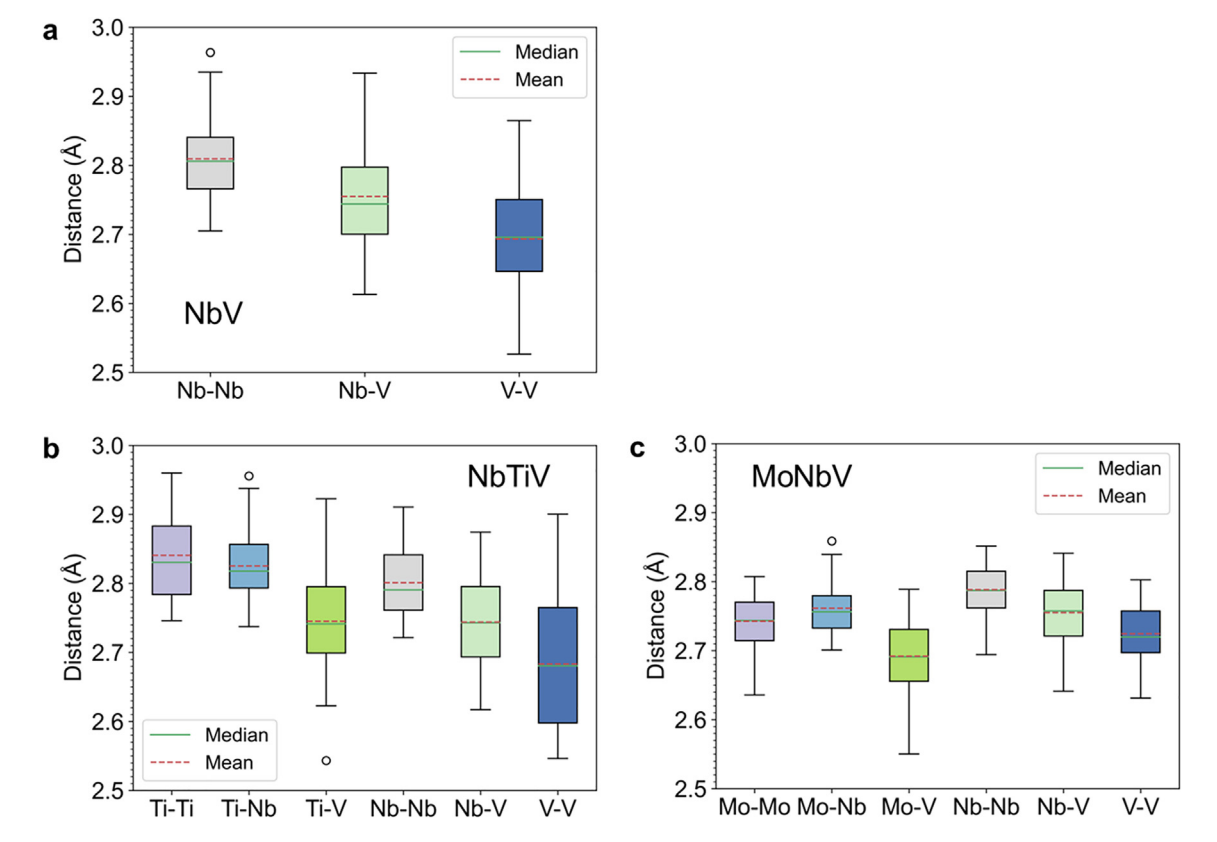


Fig. 6. Interatomic distances for the studied alloys. (**a-c**) box and whisker plots showing the spread of 1NN distances for different atomic species pairs present in NbV, NbTiV, and MoNbV alloys respectively. The box region represents the 25th to 75th percentile, the whisker extends to either the 1.5 times inter-quartile ranges or the maximum and minimum values, and the empty circles represent outliers beyond 1.5 times the inter-quartile range. The median and mean for each type of atomic bonds are exhibited as the green solid line and red dashed line, respectively. (For interpretation of the references to colour in this figure legend, the reader is referred to the web version of this article.)

Table 2Changes in the elastic constants (GPa) as going from NbV to NbTiV or MoNbV. NbV_{Ti} and NbV_{Mo} stand for the effect of Ti and Mo on the elastic constants of NbV. Results are shown from the neutron-diffraction data.

Alloys	△C ₁₁ (GPa)	ΔC_{12} (GPa)	△C ₄₄ (GPa)	$\Delta(C_{12} - C_{44})$	ΔA_z	∆E (GPa)	⊿G (GPa)	<i>∆B</i> (GPa)	Δv	∆B/G
NbV _{Ti} NbV _{Mo}	-62.3 115.6	-25.3 44.8	3.6 15.0	-28.9 29.8	$0.40 \\ -0.07$	-12.3 58.2	-3.9 21.4	-37.6 69.3	$-0.021 \\ -0.006$	-0.62 -0.22

Table 3The elastic constants (C_{ij}/GPa), Cauchy pressure (C_{12} - C_{44}/GPa), Zener anisotropy ratio (A_Z), Young's modulus (E/GPa), shear modulus (E/GPa), bulk modulus (E/GPa), Poisson's ratio (v), and E/GPa0, Poisson's ratio (v), and E/GPa1, shear modulus (E/GPa2), bulk modulus (E/GPa3), Poisson's ratio (v), and E/GPa3, shear modulus (E/GPa3), bulk modulus (E/GPa3), Poisson's ratio (v), and E/GPa3, shear modulus (E/GPa3), bulk modulus (E/GPa3), Poisson's ratio (v), and E/GPa3, shear modulus (E/GPa3), bulk modulus (E/GPa3), Poisson's ratio (v), and E/GPa3, shear modulus (E/GPa3), bulk modulus (E/GPa3), Poisson's ratio (v), and E/GPa3, shear modulus (E/GPa3), bulk modulus (E/GPa3), Poisson's ratio (v), and E/GPa3, shear modulus (E/GPa3), bulk modulus (E/GPa3), Poisson's ratio (v), and E/GPa3, shear modulus (E/GPa3), bulk modulus (E/GPa3), Poisson's ratio (v), and E/GPa3, ratio (v), and E/GPa4, ratio (

Alloys	C ₁₁	C ₁₂	C ₄₄	C ₁₂ - C ₄₄	A_z	Е	G	В	ν	B/G
NbV ^a	226.7	117.4	32.0	85.4	0.59	109.7	39.7	153.8	0.381	3.87
NbTiV ^a	164.4	92.1	35.6	56.5	0.99	97.4	35.8	116.2	0.360	3.25
MoNbV ^a	342.3	162.2	47.0	115.2	0.52	167.9	61.1	223.1	0.375	3.65
AlMoNbV [44] ^b	261.4	117.9	52.4	65.5	1.57	159.3	59.4	165.7	0.340	2.79
CrMoNbV [6] ^a	341.0	141.8	59.0	82.8	0.60	195.7	72.8	208.2	0.343	2.86
HfNbTiVZr [46] ^b	145.3	85.4	70.0	15.4	2.34	129.1	49.8	105.4	0.296	2.12
NbTaTiV [45] ^a	196.8	121.4	46.7	74.7	1.24	117.3	42.9	146.6	0.368	3.42
NbTiVZr [48] ^b	166.4	94.7	53.8	40.9	1.50	121.1	45.7	118.6	0.330	2.60
MoNbTaW [47] ^c	392	158	79	79	0.68	245	92	236	0.327	2.56
MoNbTaVW [47] ^c	379	143	65	78	0.55	200	82	222	0.348	2.71
MoNbTaTiV[49] ^d	303.5	135.9	22.6	113.3	0.78	130.5	47.1	190	0.386	4.04
MoNbTiV [50] ^b	265.5	114.0	51.7	62.3	0.68	161.1	60.3	164.5	0.337	2.73
MoNbTiZr [48] ^b	209.9	101.0	52.6	48.4	0.97	141.7	53.3	137.3	0.328	2.58
MoNbTiVZr [48] ^b	213.7	100.7	50.9	49.8	0.90	141.1	53.2	138.5	0.330	2.61
Mo [64] ^a	469.6	167.6	106.8	60.8	0.71	319.5	122.7	268.3	0.302	2.19
Nb [43] ^a	246	134	28.7	105.3	0.51	105.2	37.6	171.3	0.398	4.56
Ti (bcc at 1000 °C) [65] ^a	97.7	82.7	37.5	45.2	5	55.7	20.0	87.7	0.394	4.39
V [43] ^a	228	119	42.6	76.4	0.78	128.1	47.0	155.3	0.363	3.30

^a Experiment.

may be more brittle, in spite of possibly having higher strength [66]. However, when adding Ta to NbTiV alloy to form the NbTaTiV alloy, the value of the *B/G* ratio has almost no change, indicating that the brittle/ductile character of the NbTiV host might not change much, which is supported by the observed tensile ductility of NbTaTiV [67]. In fact, adding Ta to NbV does not change the brittle/ductile character of the host alloy, according to a recent work [68]. A similar effect could be also seen when alloying Hf into NbTiV, because of the observed good tensile ductility [69], although the information of elastic constants is absent for the HfNbTiV alloy.

So far, a significant barrier in the development of useful RHEAs is the lack of tensile ductility at RT, which hinders their engineering application. Based on the above discussion, we can expect that ductile RHEAs could be designed based on the binary NbV or ternary NbTiV alloys by rationally adjusting their chemical compositions that are not limited to the equiatomic ratios. Moreover, due to the insensitive temperature dependence of elastic constants of Nb and V, a stable high-temperature strength can also be ensured [6]. When designing such ductile RHEAs, suitable alloying elements can be considered to be added for the strengthening effect. For example, it can be expected that reasonable contents of Ta and Hf with large atomic radii could be added for strengthening, which could not deteriorate the ductility too much. Also, other elements, such as Al, Cr, Mo, and Zr, could be considered for strengthening by introducing large atomic-size and modulus mismatches and a suitable degree of SRO. Of course, the caveat of adding these elements is the cost of ductility. Moreover, for high-temperature applications, elements that can improve oxidation resistance can be considered as well, such as Al, Cr, and Si [6,70].

4. Conclusions

The present work studies the elastic constants of the equiatomic NbV, NbTiV, and MoNbV, refractory multi-principalelement alloys, using in-situ neutron diffraction and firstprinciples calculations. A good agreement of the experimentallymeasured and theoretically-calculated elastic constants, such as Young's modulus, shear modulus, bulk modulus, and Poisson's ratio, are found for the three alloys. Among these alloys, the NbTiV alloy exhibits a nearly perfect elastic isotropy with a VEC value of \sim 4.7, suggesting that the VEC values could provide useful guidance to design the elastically isotropic HEA, although it depends on the specific alloy system. The alloying effect of adding Ti and Mo into the NbV on the elastic constants is discussed. It was found that the addition of Ti into NbV causes a decrease in C_{11} and C_{12} , and a slight increase in C₄₄, while the addition of Mo into the NbV leads to the strongly enhanced C_{11} , C_{12} , and C_{44} . The brittle/ductile characteristics of the studied alloys are also predicted with Pugh's ratio (B/G), Cauchy pressure (C_{12} - C_{44}), and Poisson's ratio (ν), which are supported by experimental observations. Furthermore, valuable insights are provided to design ductile and strong RHEAs, based on the understanding of the alloying effect on elastic constants and mechanical performance in light of the present and literature results.

5. Data availability

The data that support the findings of this study are available from the corresponding author upon reasonable request.

^b Coherent potential approximation (CPA).

^c Special quasi-random structure (SQS).

d Maximum Entropy (MaxEnt).

Declaration of Competing Interest

The authors declare that they have no known competing financial interests or personal relationships that could have appeared to influence the work reported in this paper.

Acknowledgments

R. Feng thanks for the support from the Materials and Engineering Initiative at the Spallation Neutron Source (SNS), Oak Ridge National Laboratory (ORNL). The present research used resources at the SNS, a U.S. Department of Energy (DOE) Office of Science User Facility operated by the ORNL. P. K. Liaw appreciates the support from (1) the National Science Foundation (DMR-1611180 and 1809640) with program directors, Drs. J. Yang, G. Shiflet, and D. Farkas and (2) the US Army Research Office (W911NF-13-1-0438 and W911NF-19-2-0049) with program managers, Drs. M.P. Bakas, S.N. Mathaudhu, and D.M. Stepp. G.K. and W.C. acknowledge the support by the National Science Foundation under Grant No. DMR-1945380. This work used the Extreme Science and Engineering Discovery Environment (XSEDE), which is supported by National Science Foundation grant number ACI-1548562. This research used resources of the National Energy Research Scientific Computing Center (NERSC), a U.S. Department of Energy Office of Science User Facility located at Lawrence Berkeley National Laboratory, operated under Contract No. DE-AC02-05CH11231.

Appendix A. Supplementary material

Supplementary data to this article can be found online at https://doi.org/10.1016/j.matdes.2022.110820.

References

- [1] J.W. Yeh, S.K. Chen, S.J. Lin, J.Y. Gan, T.S. Chin, T.T. Shun, C.H. Tsau, S.Y. Chang, Nanostructured high-entropy alloys with multiple principal elements: novel
- alloy design concepts and outcomes, Adv. Eng. Mater. 6 (5) (2004) 299–303.

 [2] B. Cantor, I. Chang, P. Knight, A. Vincent, Microstructural development in equiatomic multicomponent alloys, Mater. Sci. Eng. A 375 (2004) 213–218.
- [3] D.B. Miracle, O.N. Senkov, A critical review of high entropy alloys and related concepts, Acta Mater. 122 (2017) 448–511.
- [4] E.P. George, D. Raabe, R.O. Ritchie, High-entropy alloys, Nat. Rev. Mater. 4 (8) (2019) 515-534.
- [5] Y. Zhang, T.T. Zuo, Z. Tang, M.C. Gao, K.A. Dahmen, P.K. Liaw, Z.P. Lu, Microstructures and properties of high-entropy alloys, Prog. Mater. Sci. 61 (2014) 1–93.
- [6] R. Feng, B. Feng, M.C. Gao, C. Zhang, J.C. Neuefeind, J.D. Poplawsky, Y. Ren, K. An, M. Widom, P.K. Liaw, Superior high-temperature strength in a supersaturated refractory high-entropy alloy, Adv. Mater. 33 (48) (2021) 2102401.
- [7] P. Shi, R. Li, Y. Li, Y. Wen, Y. Zhong, W. Ren, Z. Shen, T. Zheng, J. Peng, X. Liang, P. Hu, N. Min, Y. Zhang, Y. Ren, P.K. Liaw, D. Raabe, Y.-D. Wang, Hierarchical crack buffering triples ductility in eutectic herringbone high-entropy alloys, Science 373 (6557) (2021) 912–918.
- [8] T. Yang, Y.L. Zhao, Y. Tong, Z.B. Jiao, J. Wei, J.X. Cai, X.D. Han, D. Chen, A. Hu, J.J. Kai, K. Lu, Y. Liu, C.T. Liu, Multicomponent intermetallic nanoparticles and superb mechanical behaviors of complex alloys, Science 362 (6417) (2018) 933-937
- [9] Z. Lei, X. Liu, Y. Wu, H. Wang, S. Jiang, S. Wang, X. Hui, Y. Wu, B. Gault, P. Kontis, D. Raabe, L. Gu, Q. Zhang, H. Chen, H. Wang, J. Liu, K. An, Q. Zeng, T.-G. Nieh, Z. Lu, Enhanced strength and ductility in a high-entropy alloy via ordered oxygen complexes, Nature 563 (7732) (2018) 546–550.
- [10] Q. Pan, L. Zhang, R. Feng, Q. Lu, K. An, C. Chuang Andrew, D. Poplawsky Jonathan, K. Liaw Peter, L. Lu, Gradient cell-structured high-entropy alloy with exceptional strength and ductility, Science 374 (6570) (2021) 984–989.
- [11] W. Li, D. Xie, D. Li, Y. Zhang, Y. Gao, P.K. Liaw, Mechanical behavior of highentropy alloys, Prog. Mater Sci. 118 (2021) 100777.
- [12] R. Feng, Y. Rao, C. Liu, X. Xie, D. Yu, Y. Chen, M. Ghazisaeidi, T. Ungar, H. Wang, K. An, P.K. Liaw, Enhancing fatigue life by ductile-transformable multicomponent B2 precipitates in a high-entropy alloy, Nat. Commun. 12 (1) (2021) 3588.
- [13] B. Gludovatz, A. Hohenwarter, D. Catoor, E.H. Chang, E.P. George, R.O. Ritchie, A fracture-resistant high-entropy alloy for cryogenic applications, Science 345 (6201) (2014) 1153–1158.

- [14] Y. Shi, L. Collins, R. Feng, C. Zhang, N. Balke, P.K. Liaw, B. Yang, Homogenization of AlxCoCrFeNi high-entropy alloys with improved corrosion resistance, Corros. Sci. 133 (2018) 120–131.
- [15] Y. Shi, B. Yang, P. Liaw, Corrosion-resistant high-entropy alloys: A review, Metals 7 (2) (2017) 43.
- [16] T. Zuo, M.C. Gao, L. Ouyang, X. Yang, Y. Cheng, R. Feng, S. Chen, P.K. Liaw, J.A. Hawk, Y. Zhang, Tailoring magnetic behavior of CoFeMnNiX (X = Al, Cr, Ga, and Sn) high entropy alloys by metal doping, Acta Mater. 130 (2017) 10–18.
- [17] T. Zuo, M. Zhang, P.K. Liaw, Y. Zhang, Novel high entropy alloys of FexCo1xNiMnGa with excellent soft magnetic properties, Intermetallics 100 (2018) 1–8
- [18] Y. Ma, Q. Wang, X. Zhou, J. Hao, B. Gault, Q. Zhang, C. Dong, T.G. Nieh, A novel soft-magnetic B2-based multiprincipal-element alloy with a uniform distribution of coherent body-centered-cubic nanoprecipitates, Adv. Mater. 33 (14) (2021) 2006723.
- [19] H.Y. Diao, R. Feng, K.A. Dahmen, P.K. Liaw, Fundamental deformation behavior in high-entropy alloys: An overview, Curr. Opin. Solid State Mater. Sci. 21 (5) (2017) 252–266.
- [20] S. Huang, F. Tian, L. Vitos, Elasticity of high-entropy alloys from ab initio theory, J. Mater. Res. 33 (19) (2018) 2938–2953.
- [21] S.F. Pugh, Xcii., Relations between the elastic moduli and the plastic properties of polycrystalline pure metals, Lond. Edinb. Dublin philos. Mag. J. Sci. 45 (367) (1954) 823–843.
- [22] D. Pettifor, Theoretical predictions of structure and related properties of intermetallics, Mater. Sci. Technol. 8 (4) (1992) 345–349.
- [23] O. Senkov, G. Wilks, J. Scott, D. Miracle, Mechanical properties of Nb25Mo25Ta25W25 and V20Nb20Mo20Ta20W20 refractory high entropy alloys, Intermetallics 19 (5) (2011) 698–706.
- [24] C. Lee, G. Song, M.C. Gao, R. Feng, P. Chen, J. Brechtl, Y. Chen, K. An, W. Guo, J.D. Poplawsky, S. Li, A.T. Samaei, W. Chen, A. Hu, H. Choo, P.K. Liaw, Lattice distortion in a strong and ductile refractory high-entropy alloy, Acta Mater. 160 (2018) 158–172.
- [25] X.L. Wang, T.M. Holden, G.Q. Rennich, A.D. Stoica, P.K. Liaw, H. Choo, C.R. Hubbard, VULCAN—The engineering diffractometer at the SNS, Phys. B: Condens. Matter 385-386(Part 1) (2006) 673-675.
- [26] K. An, H.D. Skorpenske, A.D. Stoica, D. Ma, X.-L. Wang, E. Cakmak, First in situ lattice strains measurements under load at VULCAN, Metall. Mater. Trans. A 42 (1) (2011) 95–99.
- [27] K. An, Vdrive-, Data Reduction and Interactive Visualization Software for Event Mode Neutron Diffraction, ORNL Report, Oak Ridge National, Laboratory (ORNL-TM-2012-621, (2012).).
- [28] E. Kröner, Berechnung der elastischen Konstanten des Vielkristalls aus den Konstanten des Einkristalls, Z. Phys. 151 (1958) 504-518.
- [29] H. Diao, D. Ma, R. Feng, T. Liu, C. Pu, C. Zhang, W. Guo, J.D. Poplawsky, Y. Gao, P. K. Liaw, Novel NiAl-strengthened high entropy alloys with balanced tensile strength and ductility, Mater. Sci. Eng. A 742 (2019) 636–647.
- [30] G. Kresse, J. Furthmüller, Efficient iterative schemes for ab initio total-energy calculations using a plane-wave basis set, Phys. Rev. B 54 (16) (1996) 11169–11186.
- [31] G. Kresse, J. Furthmüller, Efficiency of ab-initio total energy calculations for metals and semiconductors using a plane-wave basis set, Comput. Mater. Sci. 6 (1) (1996) 15–50.
- [32] P.É. Blöchl, Projector augmented-wave method, Physical review B 50 (24) (1994) 17953–17979.
- [33] J.P. Perdew, K. Burke, M. Ernzerhof, Generalized gradient approximation made simple, Phys. Rev. Lett. 77 (18) (1996) 3865–3868.
- [34] A. Zunger, S.H. Wei, L.G. Ferreira, J.E. Bernard, Special quasirandom structures, Phys. Rev. Lett. 65 (3) (1990) 353–356.
- [35] A. van de Walle, P. Tiwary, M. de Jong, D.L. Olmsted, M. Asta, A. Dick, D. Shin, Y. Wang, L.Q. Chen, Z.K. Liu, Efficient stochastic generation of special quasirandom structures, Calphad 42 (2013) 13–18.
- [36] M. de Jong, W. Chen, T. Angsten, A. Jain, R. Notestine, A. Gamst, M. Sluiter, C. Krishna Ande, S. van der Zwaag, J.J. Plata, C. Toher, S. Curtarolo, G. Ceder, K.A. Persson, M. Asta, Charting the complete elastic properties of inorganic crystalline compounds, Sci. Data 2 (1) (2015) 150009.
- [37] G. Kim, H. Diao, C. Lee, A.T. Samaei, T. Phan, M. de Jong, K. An, D. Ma, P.K. Liaw, W. Chen, First-principles and machine learning predictions of elasticity in severely lattice-distorted high-entropy alloys with experimental validation, Acta Mater. 181 (2019) 124-138.
- [38] R. de, Diffraction elastic constants of a cubic polycrystal, J. Appl. Crystallogr. 30 (4) (1997) 510–511.
- [39] R. Hill, The elastic behaviour of a crystalline aggregate, Proc. Phys. Soc. Section A 65 (5) (1952) 349–354.
- [40] R. Gaillac, P. Pullumbi, F.-X. Coudert, ELATE: an open-source online application for analysis and visualization of elastic tensors, J. Phys.: Condens. Matter 28 (27) (2016) 275201.
- [41] J.F. Nye, Physical properties of crystals: their representation by tensors and matrices, Oxford University Press, 1985.
- [42] K.W. Katahara, M.H. Manghnani, E.S. Fisher, Pressure derivatives of the elastic moduli of BCC Ti-V-Cr, Nb-Mo and Ta-W alloys, J. Phys. F: Met. Phys. 9 (5) (1979) 773–790.
- [43] D. Bolef, Elastic constants of single crystals of the bcc transition elements V, Nb, and Ta, J. Appl. Phys. 32 (1) (1961) 100–105.
- [44] H. Ge, F. Tian, Y. Wang, Elastic and thermal properties of refractory high-entropy alloys from first-principles calculations, Comput. Mater. Sci. 128 (2017) 185–190.

- [45] C. Lee, G. Kim, Y. Chou, B.L. Musicó, M.C. Gao, K. An, G. Song, Y.-C. Chou, V. Keppens, W. Chen, P.K. Liaw, Temperature dependence of elastic and plastic deformation behavior of a refractory high-entropy alloy, Sci. Adv. 6 (37) (2020) eaaz4748.
- [46] J.H. Dai, W. Li, Y. Song, L. Vitos, Theoretical investigation of the phase stability and elastic properties of TiZrHfNb-based high entropy alloys, Mater. Des. 182 (2019) 108033.
- [47] Y.L. Hu, L.H. Bai, Y.G. Tong, D.Y. Deng, X.B. Liang, J. Zhang, Y.J. Li, Y.X. Chen, First-principle calculation investigation of NbMoTaW based refractory high entropy alloys, J. Alloys Compd. 827 (2020) 153963.
- [48] F. Tian, L.K. Varga, N. Chen, J. Shen, L. Vitos, Ab initio design of elastically isotropic TiZrNbMoVx high-entropy alloys, J. Alloys Compd. 599 (2014) 19–25.
- [49] S.-M. Zheng, W.-Q. Feng, S.-Q. Wang, Elastic properties of high entropy alloys by MaxEnt approach, Comput. Mater. Sci. 142 (2018) 332–337.
- [50] P. Cao, X. Ni, F. Tian, L.K. Varga, L. Vitos, Ab initio study of AlxMoNbTiV highentropy alloys, J. Phys.: Condens. Matter 27 (7) (2015).
- [51] L.A. Ahlberg, O. Buck, N.E. Paton, Effects of hydrogen on anisotropic elastic properties of bcc Ti-alloys, Scr. Metall. 12 (11) (1978) 1051–1054.
- [52] T. Li, J.W. Morris, N. Nagasako, S. Kuramoto, D.C. Chrzan, "Ideal" Engineering
- Alloys, Phys. Rev. Lett. 98 (10) (2007) 105503. [53] C.N. Reid, J.L. Routbort, R.A. Maynard, Elastic constants of Ti–40 at.% Nb at 298
- °K, J. Appl. Phys. 44 (3) (1973) 1398–1399. [54] H.W. Jeong, Y.S. Yoo, Y.T. Lee, J.K. Park, Elastic softening behavior of Ti–Nb single crystal near martensitic transformation temperature, J. Appl. Phys. 108 (6) (2010).
- [55] R. Hermann, H. Hermann, M. Calin, B. Büchner, J. Eckert, Elastic constants of single crystalline β-Ti70Nb30, Scr. Mater. 66 (3–4) (2012) 198–201.
- [56] E.S. Fisher, J.F. Miller, H.L. Alberts, D.G. Westlake, Effects of hydrogen on the single-crystal elastic moduli of Nb-V and Nb-Ta solid solutions, J. Phys. F: Met. Phys. 11 (8) (1981) 1557–1576.
- [57] Y.X. Ye, B.L. Musico, Z.Z. Lu, L.B. Xu, Z.F. Lei, V. Keppens, H.X. Xu, T.G. Nieh, Evaluating elastic properties of a body-centered cubic NbHfZrTi high-entropy alloy – A direct comparison between experiments and ab initio calculations, Intermetallics 109 (2019) 167–173.
- [58] S. Schönecker, X. Li, D. Wei, S. Nozaki, H. Kato, L. Vitos, X. Li, Harnessing elastic anisotropy to achieve low-modulus refractory high-entropy alloys for biomedical applications, Mater. Des. 215 (2022) 110430.

- [59] M. Liao, Y. Liu, P. Cui, N. Qu, F. Zhou, D. Yang, T. Han, Z. Lai, J. Zhu, Modeling of alloying effect on elastic properties in BCC Nb-Ti-V-Zr solid solution: From unary to quaternary, Comput. Mater. Sci. 172 (2020) 109289.
- [60] C.-C. Yen, G.-R. Huang, Y.-C. Tan, H.-W. Yeh, D.-J. Luo, K.-T. Hsieh, E.W. Huang, J.-W. Yeh, S.-J. Lin, C.-C. Wang, C.-L. Kuo, S.-Y. Chang, Y.-C. Lo, Lattice distortion effect on elastic anisotropy of high entropy alloys, J. Alloys Compd. 818 (2020) 152876
- [61] B. Li, Y. Duan, M. Peng, H. Qi, L. Shen, X. Wang, Theoretical insights on elastic anisotropy and thermal anisotropy of TM5Al3C (TM= Zr, Hf, and Ta) carbides, Vacuum 200 (2022) 110989.
- [62] A. Yang, Y. Duan, J. Yi, C. Li, Theoretical insights into anisotropies in elastic and thermal properties of ternary β-M4AlN3 (M = V, Nb, Ta) nitrides by firstprinciples calculations, Chem. Phys. Lett. 783 (2021) 139088.
- [63] Y. Wu, C. Yang, Y. Duan, First-principles exploration of elastic anisotropy and thermal properties of the C40-type VSi2, NbSi2, and TaSi2 disilicides, Mater. Today Commun. 29 (2021) 102818.
- [64] D.I. Bolef, J. De Klerk, Elastic constants of single-crystal Mo and W between 77° and 500° K, J. Appl. Phys. 33 (7) (1962) 2311–2314.
- [65] H. Ledbetter, H. Ogi, S. Kai, S. Kim, M. Hirao, Elastic constants of bodycentered-cubic titanium monocrystals, J. Appl. Phys. 95 (9) (2004) 4642–4644.
- [66] O. Senkov, S. Senkova, D. Miracle, C. Woodward, Mechanical properties of low-density, refractory multi-principal element alloys of the Cr-Nb-Ti-V-Zr system, Mater. Sci. Eng. A 565 (2013) 51–62.
- [67] Z.Q. Xu, Z.L. Ma, Y. Tan, X.W. Cheng, Designing TiVNbTaSi refractory highentropy alloys with ambient tensile ductility, Scr. Mater. 206 (2022) 114230.
- [68] Z. Han, L. Meng, J. Yang, G. Liu, J. Yang, R. Wei, G. Zhang, Novel BCC VNbTa refractory multi-element alloys with superior tensile properties, Mater. Sci. Eng. A 825 (2021) 141908.
- [69] S. Wei, S.J. Kim, J. Kang, Y. Zhang, Y. Zhang, T. Furuhara, E.S. Park, C.C. Tasan, Natural-mixing guided design of refractory high-entropy alloys with as-cast tensile ductility, Nat. Mater. 19 (11) (2020) 1175–1181.
- [70] B. Gorr, F. Mueller, H.J. Christ, T. Mueller, H. Chen, A. Kauffmann, M. Heilmaier, High temperature oxidation behavior of an equimolar refractory metal-based alloy 20Nb20Mo20Cr20Ti20Al with and without Si addition, J. Alloys Compd. 688 (2016) 468–477.